Solar Energy
and Sustainable Development
Refereed, biannual scientific journal issued by
The Libyan Center for Solar Energy Research and Studies

Structural, Electronic, Optical, and Mechanical properties of $BaTiO_3$ Under Pressure: Using Fitting Tools to Create Predictive Functions for Mechanical Properties in Photovoltaic and 3D Printing Applications

Mohamed Karouchi[*,1], Mohamed Amhijane[2], Abdelkebir Ejjabli[1], Art Anthony Z. Munio[3], Aymane El Haji[1], Abdelmounaim Laassouli[1], Hamzaa Errahoui[1], Youssef Lachtioui[1] Omar Bajjou[1], Lhoucine Oufni[1]

[1]Laboratory of Engineering in Chemistry and Physics of Matter Faculty of Sciences and Technics, Sultan Moulay Slimane University, BP 523, 23000, Beni Mellal, Morocco.
[2]Laboratoire de Physique de Clermont Auvergne, Blaise Pascal, 63170 Aubière, France
[3]Department of Physics, Western Mindanao State University, 7000 Zamboanga City, Philippines

E-*mail:* [1]*karouchimohamed3@gmail.com*

ARTICLE INFO.

Article history:
Received 09 July 2025
Received in revised form 30 March 2026
Accepted 14 April 2026
Available online 03 May 2026

KEYWORDS

Structural properties; Electronic properties; Optical properties; Mechanical properties; Perovskite photovoltaics; Hydrostatic pressure; Photovoltaic Applications; 3D Printing Applications.

ABSTRACT

Barium titanate ($BaTiO_3$) is a representative perovskite oxide with tunable optoelectronic (and mechanical) properties, making it promising for photovoltaic and multifunctional device applications. Using density functional theory (CASTEP), we have rationally investigated its response to hydrostatic pressure (0–500 GPa) and our simulations reveal substantial lattice contraction and shortening of the Ti–O bond which involves a non-monotonic evolution of the band gap: ~1.71 eV at 0 GPa, increasing to ~ 1.94 eV at 100 GPa, and then decreasing to ~0.91 eV around 400–500 GPa. The changes also shifted the optical absorption edge into the visible light region. Device modeling using SCAPS-1D and DFT-based inputs show hypothetical efficiencies to be increased under pressure (from 15.2% at 0 GPa to ~30% at 400–500 GPa), but these volumes should be regarded as idealized. Elastic properties analysis suggests with pressure there is increased stiffness, increased ductility, and potential for mechanically resilient products.

*Corresponding author.

DOI: https://doi.org/10.51646/jsesd.v14i2.670

Overall, the results suggest that higher pressure is a parameter for tuning $BaTiO_3$ properties but would need to be verified experimentally.

الخواص البنيوية والإلكترونية والبصرية والميكانيكية لمركب $BaTiO_3$ تحت الضغط: استخدام أدوات الملاءمة لإنشاء دوال تنبؤية للخواص الميكانيكية في تطبيقات الخلايا الكهروضوئية والطباعة ثلاثية الأبعاد

محمد كروشي،محمد امحيجان، عبد الكبير الجبلي، آرت أنتوني ز. مونيو، حمزة الرحوي، أيمن الحاجي،عبد المنعم العسولي، يوسف لشتيوي، عمر باجو، الحسين اوفني

ملخص: يُعَدّ تيتانات الباريوم ($BaTiO_3$) أحد الأكاسيد ذات البنية البيروفسكايتية الممثلة، بفضل خواصه البصرية-الإلكترونية والميكانيكية القابلة للضبط، مما يجعله واعدًا في تطبيقات الخلايا الكهروضوئية والأجهزة متعددة الوظائف. باستخدام نظرية الكثافة الوظيفية (DFT) عبر برنامج CASTEP، قمنا بدراسة استجابته للضغط الهيدروستاتيكي (0–500 جيجا باسكال). تكشف المحاكاة عن انكماش كبير في الشبكة البلورية وقصر في طول الرابطة Ti–O ، مما يؤدي إلى تطور غير رتيب في فجوة الطاقة: حوالي 1.71 إلكترون فولت عند 0 جيجا باسكال، تزداد إلى ~1.94 إلكترون فولت عند 100 جيجا باسكال، ثم تنخفض إلى 0.91 إلكترون فولت في حدود 400–500 جيجا باسكال. كما أدّت هذه التغيرات إلى انتقال حافة الامتصاص البصري نحو منطقة الضوء المرئي. أظهرت نمذجة الخلية الشمسية باستخدام برنامج SCAPS-1D ومدخلات مبنية على DFT أن الكفاءة الافتراضية ترتفع تحت الضغط (من 15.2% عند 0 جيجا باسكال إلى 30٪ عند 400–500 جيجا باسكال)، إلا أن هذه القيم ينبغي اعتبارها مثالية. يشير تحليل الخواص المرنة إلى أن الضغط يزيد من الصلابة والليونة ويعزز إمكانية تصنيع منتجات ذات مقاومة ميكانيكية عالية. وبصورة عامة، تُظهر النتائج أن الضغط العالي يعدّ عاملًا فعالًا في ضبط خواص $BaTiO_3$ ، لكن الأمر يتطلب تحققًا تجريبيًا.

الكلمات المفتاحية: الخواص البنيوية؛ الخواص الإلكترونية؛ الخواص البصرية؛ الخواص الميكانيكية؛ بيروفسكايت كهروضوئي؛ الضغط الهيدروستاتيكي؛ تطبيقات كهروضوئية؛ تطبيقات الطباعة ثلاثية الأبعاد

1. INTRODUCTION

Barium titanate ($BaTiO_3$) is a perovskite oxide renowned for its exceptional ferroelectric, dielectric, and piezoelectric properties, making it a key material in advanced materials research and technological applications[1,2]. Due to its high dielectric constant, strong polarization, and wide band gap, $BaTiO_3$ is extensively used in capacitors, transducers, and electro-optic devices. More recently, its potential in photovoltaics and additive manufacturing has garnered significant interest, particularly for applications in high-efficiency solar energy conversion and 3D-printed piezoelectric components[3]. However, optimizing $BaTiO_3$'s structural, electronic, and mechanical properties for these emerging applications necessitates advanced material engineering approaches, one of which is pressure modulation[4,5].

Hydrostatic pressure is a powerful external stimulus that can significantly alter the crystal structure and electronic properties of perovskite materials[6,7]. In $BaTiO_3$, pressure-induced phase transitions from tetragonal ferroelectric to cubic paraelectric states lead to substantial modifications in its electronic structure and band gap[8,9]. While at ambient conditions $BaTiO_3$ exhibits a wide band gap of approximately 1.71 eV, applying hydrostatic pressure can alter orbital interactions and reduce the band gap, improving its optical absorption range for photovoltaic applications. This band gap tunability is crucial for enhancing charge carrier

generation and transport efficiency, key factors in achieving higher power conversion efficiency (PCE) in $BaTiO_3$-based solar cells. Moreover, pressure-driven modifications in lattice parameters impact polarization properties, further influencing its ferroelectric photovoltaic behavior[10]. Beyond optoelectronic applications, pressure also enhances the mechanical robustness of $BaTiO_3$, making it an excellent candidate for additive manufacturing and 3D printing technologies[8,11]. Conventional ceramic fabrication techniques often result in materials with inherent brittleness and porosity, limiting their functional applicability. However, pressure-assisted processing techniques such as spark plasma sintering (SPS) and cold sintering have demonstrated the ability to improve $BaTiO_3$'s densification, hardness, and fracture toughness[12]. These enhancements are essential for manufacturing high-performance piezoelectric and dielectric components via 3D printing, where structural integrity and functional reliability are paramount. Furthermore, stress-induced domain engineering under controlled pressure conditions can optimize the poling process in $BaTiO_3$ ceramics, leading to enhanced piezoelectric responses in printed devices[13,14]. Integrating pressure engineering into $BaTiO_3$-based photovoltaics and 3D printing applications presents a promising avenue for advancing next-generation energy and electronic devices[7]. By precisely tuning its structural, electronic, and mechanical properties, researchers can optimize $BaTiO_3$'s performance across multiple domains, from high-efficiency solar cells to durable, functional piezoelectric components. The study of pressure effects not only deepens the fundamental understanding of perovskite oxides but also paves the way for innovative applications in energy harvesting, smart materials, and additive manufacturing. As research in this field progresses, pressure-modulated $BaTiO_3$ is poised to play a critical role in the evolution of multifunctional ceramic technologies[6]. In light of these motivations, the present work employs first-principles calculations based on density functional theory (DFT) using the CASTEP code to systematically investigate the effects of hydrostatic pressure on the structural, electronic, optical, and mechanical properties of $BaTiO_3$. Particular attention is given to the pressure-induced modifications in lattice parameters, band structure, dielectric behavior, and elastic response. In addition, photovoltaic performance under varying pressure conditions is evaluated through device simulations using the SCAPS-1D software.

2. COMPUTATIONAL METHODE

In this study, we employed Density Functional Theory (DFT) calculations using the CASTEP code to investigate the structural, electronic, optical and mechanical properties of $BaTiO_3$ under varying pressure conditions[15–17]. CASTEP is a first-principles quantum mechanical code that utilizes a plane-wave basis set and pseudopotentials to solve the Kohn-Sham equations efficiently[15,16]. We utilized the Generalized Gradient Approximation (GGA) with the Perdew-Burke-Ernzerhof (PBE) functional to describe the exchange-correlation energy of electrons[18,19]. Ultrasoft pseudopotentials were employed to represent the interactions between valence electrons and ionic cores, allowing for a reduced plane-wave cutoff energy without compromising accuracy. A plane-wave cutoff energy of 500 eV was set to ensure convergence of the total energy and electronic properties. The Brillouin zone was sampled using a Monkhorst-Pack k-point grid of 4 × 4 × 4 for the primitive cell, providing a balance between computational cost and accuracy[20]. Structural optimizations were

performed using the Broyden-Fletcher-Goldfarb-Shanno (BFGS) algorithm, with convergence criteria set to an energy change of less than 1.0×10^{-5} eV per atom, a maximum force of 0.03 eV/Å, a maximum stress of 0.05 GPa, and a maximum displacement of 1.0×10^{-3} Å. Hydrostatic pressure was applied in increments of 50 GPa, ranging from 0 to 500 GPa, with full structural optimization at each pressure point[21]. Following geometry optimization, electronic structure calculations were conducted to obtain the band structure and density of states (DOS), providing insights into the electronic properties and band gap variations under pressure. Elastic stiffness constants (C_{ij}) were calculated using finite strain theory, from which the bulk modulus, shear modulus, Young's modulus, and Poisson's ratio were derived to assess the mechanical stability and stiffness of $BaTiO_3$ under different pressures[22].

3. DISCUSSION

3.1 Structural Properties: Crystalline Structure and XRD Analysis

3.1.1 Structural Parameters Under Pressure

In this study, first-principles calculations based on Density Functional Theory (DFT) within the CASTEP code were employed to investigate the effect of hydrostatic pressure on the structural properties of $BaTiO_3$[15,16]. By systematically varying the applied pressure, we analyzed the evolution of the lattice parameters and the unit cell volume[23]. As shown in Table 1, a clear and consistent reduction in both lattice parameters and cell volume is observed with increasing pressure. This behavior is attributed to the compression-induced densification of the crystal lattice, which in turn can significantly influence the mechanical stability and electronic characteristics of $BaTiO_3$.

Table 1: The structural evolution of $BaTiO_3$ under different pressure levels.

Pressure (GPa)	Space Group	IT Number	Lattice Parameter (Å)	Volume (Å³)	Volume Reduction %
0	PM-3M	221	4.0345	65.67032	0 %
100	PM-3M	221	3.6333	47.96272	26.99 %
200	PM-3M	221	3.4636	41.55116	36.72 %
300	PM-3M	221	3.3524	37.67623	42.63 %
400	PM-3M	221	3.2690	34.93371	46.81 %
500	PM-3M	221	3.2025	32.84486	49.99 %

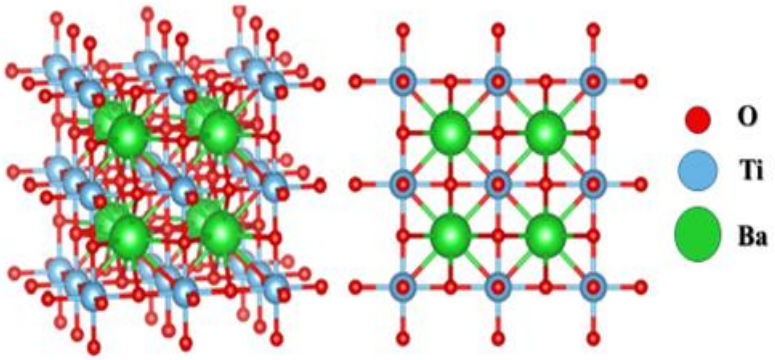

Figure.1: The perovskite super cell of $BaTiO_3$.

Despite this compression, $BaTiO_3$ remarkably preserves its cubic symmetry up to 500 GPa without undergoing any phase transition (Figure.1). This exceptional structural resilience

highlights its potential for applications in extreme environments, such as high-pressure sensors and piezoelectric devices, where maintaining crystallographic integrity is essential for ensuring reliable functional performance[24].

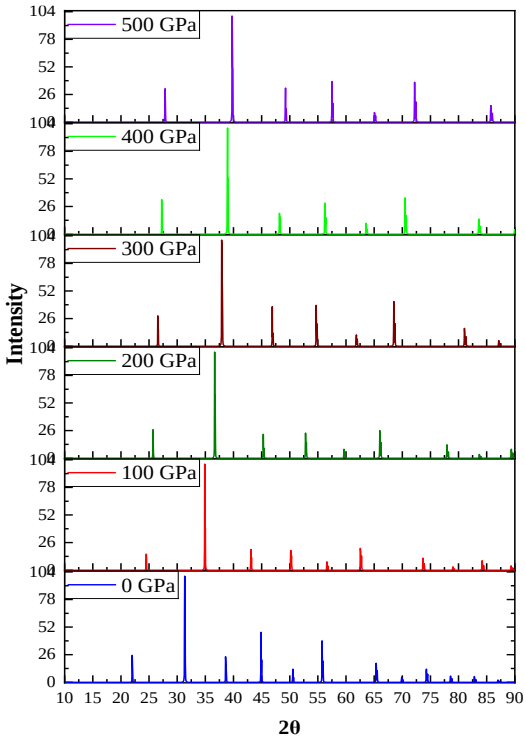

Figure.2: XRD patterns of $BaTiO_3$ under different pressure levels.

To further validate the structural evolution of $BaTiO_3$ under pressure, X-ray diffraction (XRD) simulations were carried out, as presented in Figure.2[25]. XRD analysis, a crucial tool for probing crystal symmetry and lattice variations, confirms the preservation of the cubic perovskite structure at ambient conditions, with diffraction peaks corresponding to the PM-3M space group. As pressure increases, the diffraction peaks systematically shift towards higher angles, reflecting the compression of the lattice, in agreement with the decreasing lattice parameters observed in the structural data. Moreover, at pressures exceeding 300 GPa, the broadening of the peaks suggests the onset of structural distortions, which could have significant implications for the ferroelectric and dielectric properties of $BaTiO_3$.

3.2 Electronic proprieties:

3.2.1 Optical Gap:

The electronic band gap is a fundamental parameter that governs the optical and electrical behaviour of semiconducting materials, directly influencing their suitability for applications such as photovoltaics, optoelectronics, and sensors[26,27]. In $BaTiO_3$, understanding the evolution of the band gap under pressure is essential for optimizing its functional performance[28,29]. As summarized in Table 2 and illustrated in Figure.3, the computed band gap values reveal that $BaTiO_3$ initially exhibits an indirect band gap (M–G transition) at ambient pressure (0 GPa), which evolves into a direct band gap (G–G transition) at higher pressures. Interestingly, the band gap shows a non-monotonic variation: it increases at 100 GPa

before decreasing with further pressure increments. This behaviour indicates significant electronic restructuring under compression, which could substantially affect the material's optical absorption. In particular, the gradual narrowing of the band gap at elevated pressures may enhance $BaTiO_3$'s absorption in the visible spectrum, thereby improving its potential for photovoltaic applications.

Table 2: The optical gap value evolution of $BaTiO_3$ under different pressure levels.

Pressure (GPa)	Value of Gap (GGA)	Value of Gap (HSE06)	Type of Gap	Brillion Zone
0	1.71 eV [30]	2.9 eV [30]	Indirect [30]	M-G
100	1.94 eV	3.13 eV	Direct	G-G
200	1.64 eV	2.83 eV	Direct	G-G
300	1.34 eV	2.53 eV	Direct	G-G
400	0.914 eV	2.1 eV	Direct	G-G
500	0.91 eV	2.04 eV	Direct	G-G

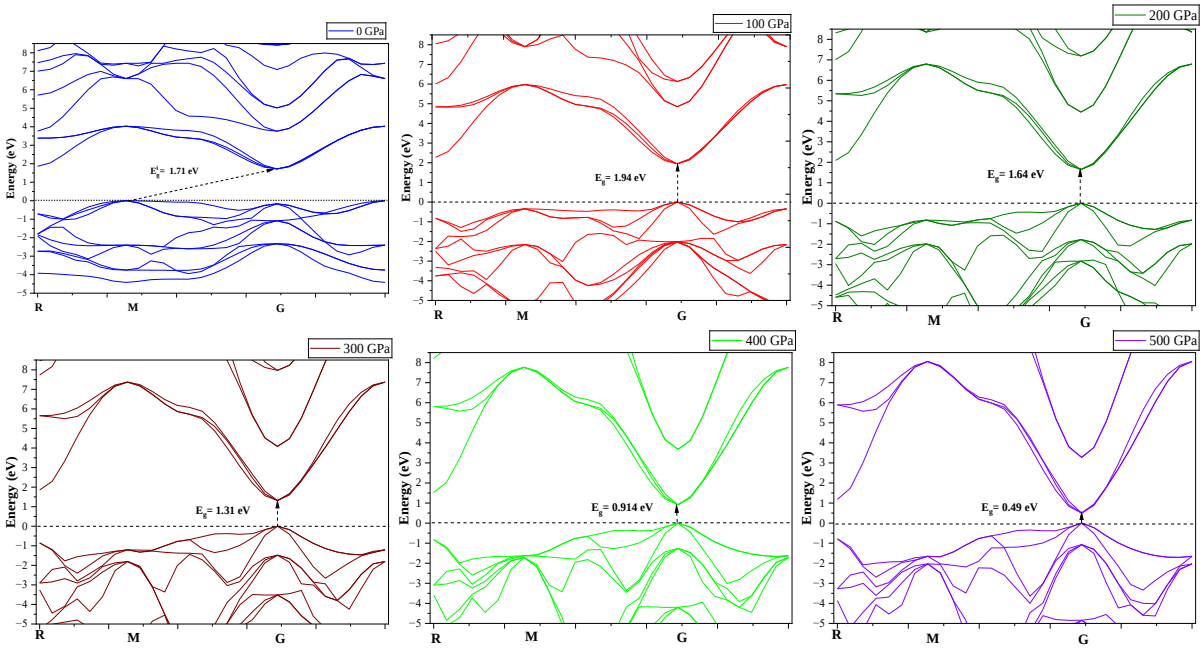

Figure.3: These figures will visualize how the band structure and density of states (DOS) change with increasing pressure.

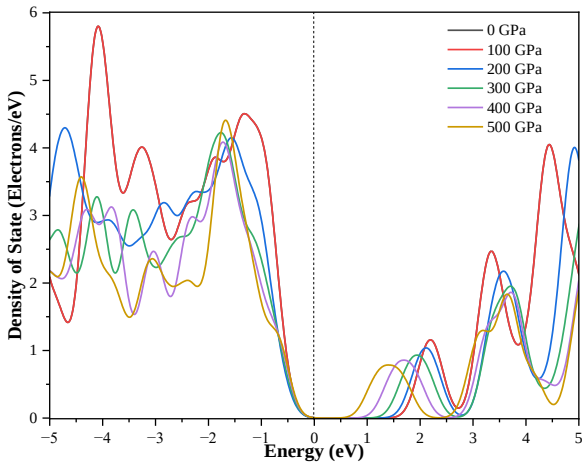

Figure.4: DOS of $BaTiO_3$ under different pressure levels.

3.2.2 Density of State

The Density of States (DOS) provides insight into the electronic structure modifications under pressure[31,32]. The DOS calculations indicate a shift in both the valence band maximum (VBM) and conduction band minimum (CBM), leading to changes in electronic dispersion. At low pressures, the valence band is predominantly composed of O 2p states, while the conduction band consists mainly of Ti 3d states. As pressure increases, the interaction between these states strengthens, contributing to band gap narrowing. Furthermore, an increase in pressure leads to a broadening of the conduction band, which suggests an enhancement in carrier mobility[33,34]. This effect is particularly important for applications in high-efficiency optoelectronic devices and pressure-sensitive semiconductors. The redistribution of electronic states under compression highlights the tunability of $BaTiO_3$'s electronic properties, reinforcing its potential use in next-generation electronic and photovoltaic materials[34,35].

3.3. Optical properties

The optical response of $BaTiO_3$ under increasing pressure conditions was examined to understand the variations in its dielectric function, refractive index, absorption coefficient, reflectivity, and energy loss function[36–38]. The following figures illustrate these properties at different pressure levels (0 GPa to 500 GPa).

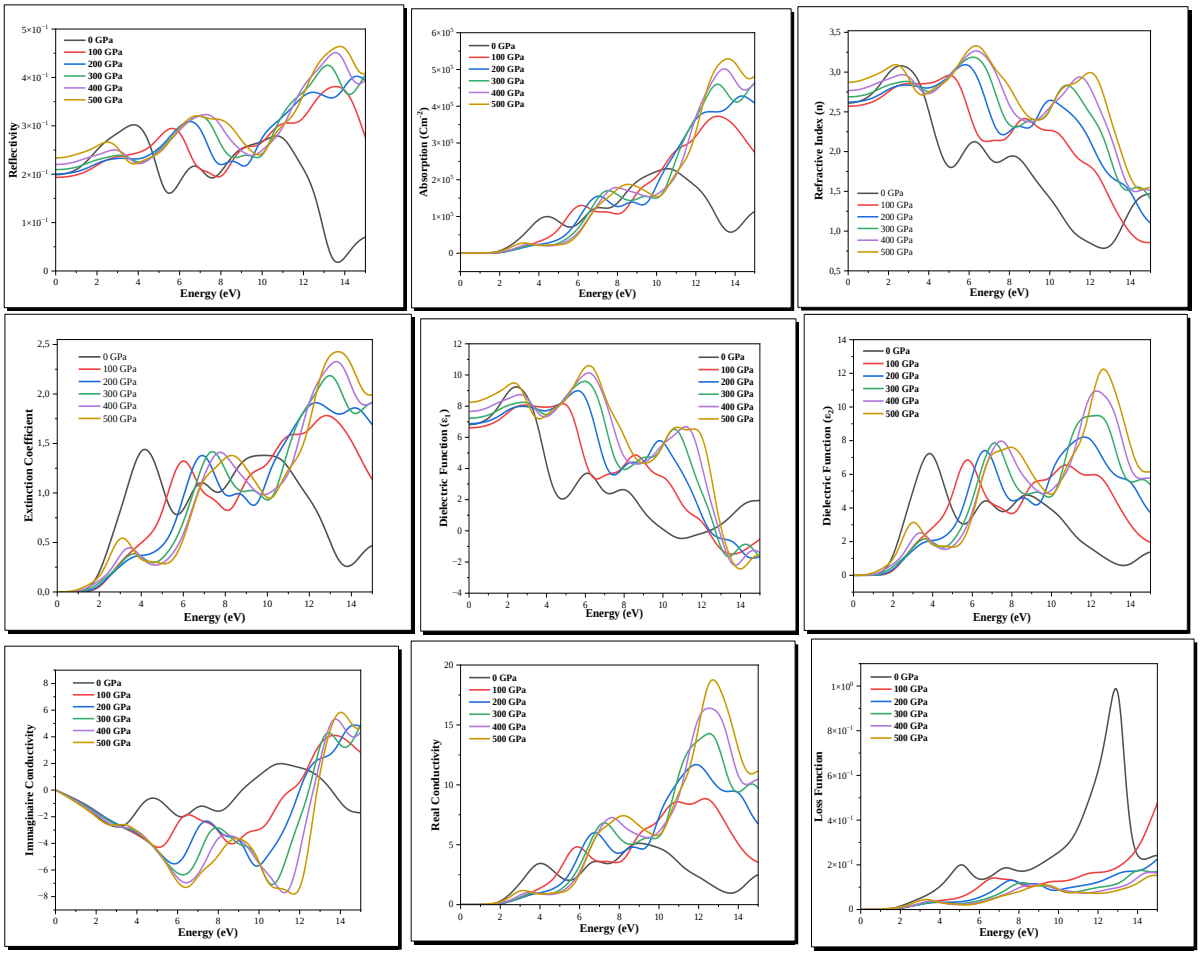

Figure.5: The optical properties of $BaTiO_3$ at various pressure levels.

Table.3: Summary of Key Optical Parameters of $BaTiO_3$ under Different Pressures.

Pression $\boldsymbol{GPa}$	0	**100**	200	300	400	500
$\boldsymbol{\varepsilon_1(0)}$ Real part of the dielectric (0 eV)	6.81	6.6	6.87	7.22	7.66	8.28
$\boldsymbol{\varepsilon_2(0)}$ Imaginary part of the dielectric function (0 eV)	0	0	0	0	0	0
$\boldsymbol{\alpha(0)}$ Absorption coefficient (0 eV)	0	0	0	0	0	0
$\boldsymbol{R(0)}$ Reflectivity (0 eV)	0.199	0.19	0.2	0.209	0.22	0.223
$\boldsymbol{\sigma_R(0)}$ Real part of optical conductivity (0 eV)	0	0	0	0	0	0
$\boldsymbol{\sigma_I(0)}$ Imaginary part of optical conductivity (0 eV)	0	0	0	0	0	0
$\boldsymbol{n(0)}$ Refractive index (0 eV)	2.61	2.57	2.62	2.68	2.76	2.82
$\boldsymbol{k(0)}$ Extinction coefficient (0 eV)	0	0	0	0	0	0
$L(\mathbf{0})$ Energy loss function (0 eV)	0	0	0	0	0	0

Both the real part $\varepsilon_1$and the imaginary part ε_2 of the dielectric function are important and provide crucial information about the electrical and optical behavior of a material. The real part of the dielectric function is related to the electrical properties and the ability of the material to polarize [39,40], while the imaginary part is associated with the energy dissipation and optical properties of the material. Together, these two parts provide a complete picture of the dielectric behavior of the material [41,42].

$$\varepsilon(\omega) = \varepsilon_1(\omega) + i\varepsilon_2(\omega) \tag{1}$$

The $\mathrm{Kramers} - \mathrm{Kronig}$ relation enables the acquisition of the real component:

$$\varepsilon_1(\omega) = 1 + \frac{2}{\pi} M \int_0^{\infty} \frac{\varepsilon_2(\omega')\omega'}{\omega'^2 - \omega^2} d\omega \tag{2}$$

The symbol M in the aforementioned equation represents the principal part value of the integral. The imaginary component is determined by the $\mathrm{Kohn\ Sham}$ equation that pertains to the relevant particles. The determination of the imaginary part, in contrast, is contingent upon the $\mathrm{Kohn\ Sham}$ equation particle[43,44]:

$$\varepsilon_2(\omega) = \frac{Ve^2}{2\pi\hbar m^2\,\omega^2} \int d^3k \sum_{nm'} \left|\langle kn|p|kn\rangle'\right|^2 f(kn) \times (1 - f(kn'))\delta\left(E_{kn} - E_{kn'} - \hbar\omega\right) \tag{3}$$

The determination of polarization $P(\omega)$ and susceptibility $\chi(\omega)$ in Perovskite materials involves utilizing the real component of dielectric parameters. This relationship allows for the characterization and quantification of the material's response to an applied electric field, shedding light on its polarization behavior. The $\mathrm{real\ part}$ of dielectric function $\varepsilon_1(\omega)$ parameters serves as a key metric in understanding how Perovskite materials interact with external electric fields, offering insights into their dielectric properties and susceptibility to polarization under specific conditions[45,46]:

$$P(\omega) = \varepsilon_0 E(\omega) = [\varepsilon_1(\omega) - 1]\varepsilon_0 E(\omega) \tag{4}$$

Index of Refraction; The material's refractive index is directly linked to the real segment of the dielectric function. The refractive index (n) can be expressed as $n = \sqrt{\varepsilon_1}$, representing how light travels through the material[40,47].

The optical properties of $BaTiO_3$ under varying pressure conditions were systematically investigated to better understand its optoelectronic behavior. Figure.5($\varepsilon_1(\omega)$) presents the real part of the dielectric function ($\varepsilon_1(\omega)$) as a function of photon energy, where at ambient pressure (0 GPa), a pronounced peak appears at low energy, indicating strong polarization effects. As pressure increases, this peak shifts towards higher photon energies, reflecting a denser electronic environment that enhances interband transitions. This shift is consistent with the reduction in band gap observed under compression, confirming an increase in electronic transitions at lower wavelengths. The imaginary part of the dielectric function ($\varepsilon_2(\omega)$), depicted in Figure.5($\varepsilon_2(\omega)$), provides further insight into the material's absorption behavior. At 0 GPa, $\varepsilon_2(\omega)$ displays an absorption edge near the band gap energy (1.71 eV). With rising pressure, the peak intensity slightly decreases, and the absorption onset moves towards lower photon energies, a trend that correlates with the narrowing band gap and suggests enhanced absorption in the visible spectrum, favorable for photovoltaic applications[48]. Complementing these findings, the refractive index (n) behavior is illustrated in Figure.5(n). At ambient pressure, $BaTiO_3$ exhibits a high refractive index at low photon energies, which diminishes at higher energies. Under compression, the static refractive index increases, especially at lower energies, due to the denser electronic structure.

This study reveals that pressure significantly modifies the optical properties of $BaTiO_3$, with implications for photovoltaics and other optoelectronic applications. The extinction coefficient (k,Figure. 5) follows the same pressure-dependent trend as the imaginary dielectric function, showing a redshift and enhanced absorption strength that indicate a greater density of states available for electronic transitions. The absorption coefficient (α, Fig. 5) rises steeply beyond the band gap at 0 GPa, while increasing pressure shifts the absorption edge to lower photon energies, confirming tunability of $BaTiO_3$ for solar cell applications. Reflectivity (R, Fig. 5) decreases at high photon energies but is enhanced at low energies under compression, suggesting stronger interband interactions and potential use in optical coatings. The energy loss function (L, Fig. 5) exhibits a plasma resonance peak that shifts to higher energies with pressure, reflecting increased electronic density and reduced free-carrier screening—factors relevant for plasmonic devices. Optical conductivity (σ, Fig. 5) also increases at lower energies with pressure, pointing to a pressure-driven trend toward semimetallic behavior. Together, these observations highlight that compression enhances light absorption, modifies plasmonic responses, and improves conductivity, thereby reinforcing $BaTiO_3$'s promise not only for photovoltaics but also for advanced optical coatings, waveguides, and photonic crystals. A summary of the key optical parameters under different pressures is provided in Table 3.

3.4 Elastic propriety

The stiffness matrices calculated at various pressures reveal a pronounced enhancement in the elastic response of $BaTiO_3$ under compression (Table 4)[49,50]. At 0 GPa, the diagonal elements of the stiffness matrix are around 266.61 GPa (for the cubic components) and 118.68 GPa (for the shear components). As pressure increases to 100, 200, 300, 400, and 500 GPa, these values rise dramatically for instance, reaching up to 3054.5 GPa and 380.49 GPa at 500 GPa. This significant increase indicates that $BaTiO_3$ becomes substantially stiffer with

applied pressure, a key characteristic for applications in 3D printing where high structural integrity and resistance to deformation are essential.

Table. 4: Stiffness matrix of $BaTiO_3$ under different pressure levels.

stiffness matrix (coefficients in 0 GPa)	stiffness matrix (coefficients in 100 GPa)
266.61 96.795 96.795 0 0 0	935.66 324.42 324.42 0 0 0
96.795 266.61 96.795 0 0 0	324.42 935.66 324.42 0 0 0
96.795 96.795 266.61 0 0 0	324.42 324.42 935.66 0 0 0
0 0 0 118.68 0 0	0 0 0 213.99 0 0
0 0 0 0 118.68 0	0 0 0 0 213.99 0
0 0 0 0 0 118.68	0 0 0 0 0 213.99
stiffness matrix (coefficients in 200 GPa)	**stiffness matrix (coefficients in 300 GPa)**
1530.1 519.09 519.09 0 0 0	2046.8 728.65 728.65 0 0 0
519.09 1530.1 519.09 0 0 0	728.65 2046.8 728.65 0 0 0
519.09 519.09 1530.1 0 0 0	728.65 728.65 2046.8 0 0 0
0 0 0 276.73 0 0	0 0 0 329.75 0 0
0 0 0 0 276.73 0	0 0 0 0 329.75 0
0 0 0 0 0 276.73	0 0 0 0 0 329.75
Stiffness matrix (coefficients in 400 GPa)	**Stiffness matrix (coefficients in 500 GPa)**
2595.2 920.56 920.56 0 0 0	3054.5 1077.8 1077.8 0 0 0
920.56 2595.2 920.56 0 0 0	1077.8 3054.5 1077.8 0 0 0
920.56 920.56 2595.2 0 0 0	1077.8 1077.8 3054.5 0 0 0
0 0 0 361.33 0 0	0 0 0 380.49 0 0
0 0 0 0 361.33 0	0 0 0 0 380.49 0
0 0 0 0 0 361.33	0 0 0 0 0 380.49

Table. 5: Average properties of $BaTiO_3$ under different pressure levels.

Value of Pressure	Averaging scheme	Bulk modulus	Young's modulus	Shear modulus	Poisson's ratio
0 GPa	Voigt	K_V = 153.4 GPa	E_V = 256.83 GPa	G_V = 105.17 GPa	ν_V = 0.22096
	Reuss	K_R = 153.4 GPa	E_R = 251.27 GPa	G_R = 102.39 GPa	ν_R = 0.227
	Hill	K_H = 153.4 GPa	E_H = 254.05 GPa	G_H = 103.78 GPa	ν_H = 0.22397
100 GPa	Voigt	K_V = 528.17 GPa	E_V = 649.23 GPa	G_V = 250.64 GPa	ν_V = 0.29513
	Reuss	K_R = 528.17 GPa	E_R = 632.41 GPa	G_R = 243.15 GPa	ν_R = 0.30044
	Hill	K_H = 528.17 GPa	E_H = 640.84 GPa	G_H = 246.9 GPa	ν_H = 0.29778
200 GPa	Voigt	K_V = 856.09 GPa	E_V = 966.19 GPa	G_V = 368.24 GPa	ν_V = 0.3119
	Reuss	K_R = 856.09 GPa	E_R = 895.84 GPa	G_R = 337.9 GPa	ν_R = 0.32559
	Hill	K_H = 856.09 GPa	E_H = 931.2 GPa	G_H = 353.07 GPa	ν_H = 0.31871
300 GPa	K_V = 1168 GPa	E_V = 1223.3 GPa	G_V = 461.48 GPa	ν_V = 0.32544	K_V = 1168 GPa
	K_R = 1168 GPa	E_R = 1106.2 GPa	G_R = 412.12 GPa	ν_R = 0.34215	K_R = 1168 GPa
	K_H = 1168 GPa	E_H = 1165.2 GPa	G_H = 436.8 GPa	ν_H = 0.33374	K_H = 1168 GPa
400 GPa	Voigt	K_V = 1478.8 GPa	E_V = 1472.1 GPa	G_V = 551.72 GPa	ν_V = 0.33409
	Reuss	K_R = 1478.8 GPa	E_R = 1269.2 GPa	G_R = 467.67 GPa	ν_R = 0.35695
	Hill	K_H = 1478.8 GPa	E_H = 1371.5 GPa	G_H = 509.7 GPa	ν_H = 0.34542
500 GPa	Voigt	K_V = 1736.7 GPa	E_V = 1670.9 GPa	G_V = 623.65 GPa	ν_V = 0.33965
	Reuss	K_R = 1736.7 GPa	E_R = 1380.2 GPa	G_R = 504.64 GPa	ν_R = 0.36754
	Hill	K_H = 1736.7 GPa	E_H = 1527.1 GPa	G_H = 564.14 GPa	ν_H = 0.35345

The averaged elastic properties obtained using Voigt, Reuss, and Hill schemes, further quantify this improvement (Table 5)[51,52]. At ambient conditions, the bulk modulus is about

153.4 GPa, Young's modulus is approximately 254.05 GPa, and the shear modulus is around 103.78 GPa. Under increased pressure, these moduli show a marked enhancement, with the bulk modulus rising to 1736.7 GPa, Young's modulus to 1527.1 GPa, and the shear modulus to 564.14 GPa at 500 GPa. The modest increase in Poisson's ratio from roughly 0.224 to 0.35345 suggests that while the material becomes much stiffer, it still retains some ductility. This balance between stiffness and ductility is particularly advantageous for 3D printing applications, where the material must withstand mechanical stresses without fracturing during the fabrication process[53–55].

3.5. Elastic Moduli vs Pressure Analysis

Equations plots describing the variation of elastic moduli with pressure for the Hill averaging scheme as represented in Figure.7[56,57].

Bulk Modulus: $K(P) = 156.1497 + 3.7670P - 1.2661 \times 10^{-3}P^2 + 1.3380 \times 10^{-7}P^3$

Young's Modulus: $E(P) = 256.1428 + 4.2432P - 4.8496 \times 10^{-3}P^2 + 2.9132 \times 10^{-6}P^3$

Shear Modulus: $G(P) = 104.5059 + 1.5830P - 1.9133 \times 10^{-3}P^2 + 1.1785 \times 10^{-6}P^3$

Poisson's Ratio: $\nu(P) = 0.2329 + 0.0006P - 6.5339 \times 10^{-7}P^2$

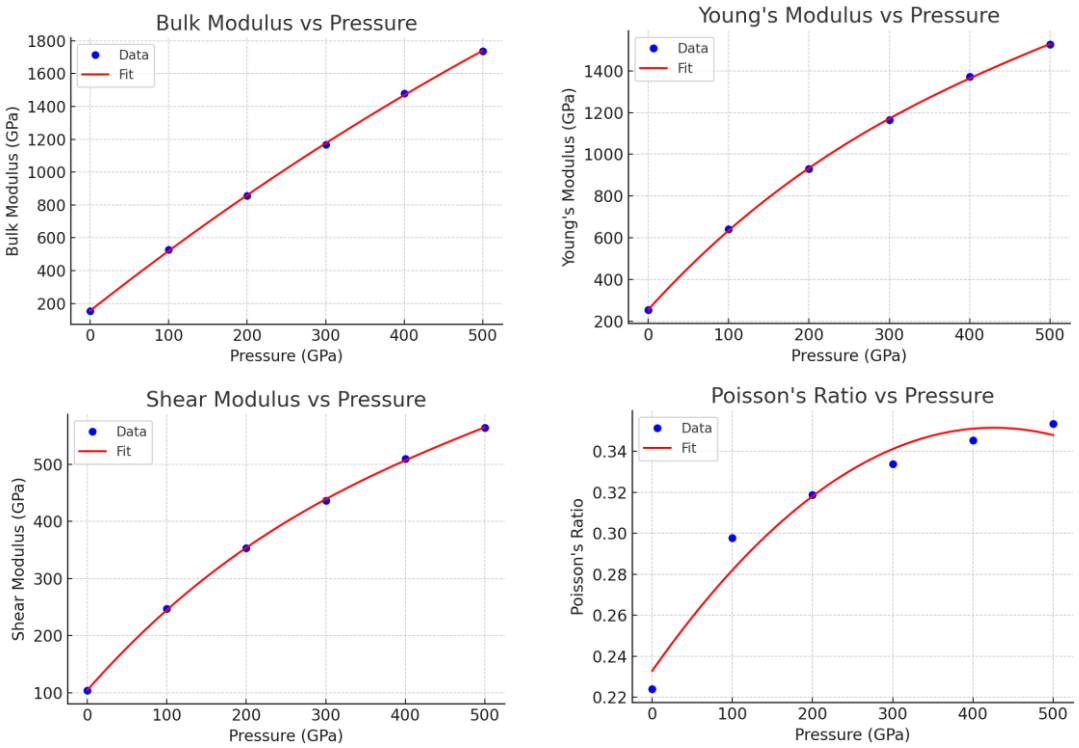

Figure.7: Fitting of Poisson's Ratio vs Pressure, Young's Modulus vs Pressure, Shear Modulus vs Pressure, and Bulk Modulus vs Pressure

To further understand the pressure dependence of these properties, predictive polynomial functions were developed for the elastic moduli[58,59].

Bulk Modulus K(P): $K(P) = 156.1497 + 3.7670P - 1.2661\times10^{-3}P^2 + 1.3380\times10^{-7}P^3$

This equation shows that as pressure (P) increases, the bulk modulus increases nonlinearly. A higher bulk modulus indicates that $BaTiO_3$ becomes more resistant to uniform compression, implying improved structural integrity under load.

Young's Modulus E(P): $E(P) = 256.1428 + 4.2432P - 4.8496\times10^{-3}P^2 + 2.9132\times10^{-6}P^3$

Similarly, Young's modulus increases with pressure, which means the material becomes stiffer and can better resist tensile forces. This stiffness is critical in applications where deformation under stress must be minimized.

Shear Modulus G(P): $G(P) = 104.5059 + 1.5830P - 1.9133\times10^{-3}P^2 + 1.1785\times10^{-6}P^3$

The shear modulus also increases with pressure, indicating enhanced resistance to shape changes under shear stress. This property is particularly important for ensuring the stability of the material when subjected to twisting or bending forces.

Poisson's Ratio ν(P): $\nu(P) = 0.2329 + 0.0006P - 6.5339\times10^{-7}P^2$

The slight increase in Poisson's ratio with pressure suggests a modest change in lateral expansion relative to axial compression, reflecting the material's ductility and the balance between stiffness and flexibility.with similar predictive functions established for Young's modulus, shear modulus, and Poisson's ratio. These fitted equations not only capture the observed trends but also serve as valuable tools for forecasting the mechanical behavior of $BaTiO_3$ under conditions that extend beyond our simulation range. This predictive capability is crucial for optimizing the material's performance in advanced manufacturing processes such as 3D printing, where precise control over mechanical properties is required.

3.6. Interpretation and Application in 3D Printing:

These predictive models reveal that pressure significantly enhances the mechanical properties of $BaTiO_3$, making it a highly promising material for 3D printing applications[60–62]. In 3D printing, particularly in the fabrication of functional components and structural elements, materials are required to exhibit high stiffness and durability while maintaining sufficient ductility to prevent brittle failure[63]. The increasing bulk, Young's, and shear moduli under pressure imply that $BaTiO_3$ can be engineered to have superior load-bearing capacity and resistance to deformation. Moreover, the fitted equations enable precise prediction and tailoring of these properties at different processing conditions, allowing for optimization of the printing parameters to achieve components with desired mechanical performance. Consequently, these results underscore the potential of pressure-engineered $BaTiO_3$ for advanced manufacturing processes, where enhanced mechanical robustness is essential for high-performance 3D printed structures[64].

Table 6: Eigenvalues of the stiffness matrix of $BaTiO_3$ under different pressure levels

Pressure	λ_1	λ_2	λ_3	λ_4	λ_5	λ_6
0 GPa	118.68 GPa	118.68 GPa	118.68 GPa	169.81 GPa	169.81 GPa	460.2 GPa
100 GPa	213.99 GPa	213.99 GPa	213.99 GPa	611.24 GPa	611.24 GPa	1584.5 GPa
200 GPa	276.73 GPa	276.73 GPa	276.73 GPa	1011 GPa	1011 GPa	2568.3 GPa
300 GPa	329.75 GPa	329.75 GPa	329.75 GPa	1318.2 GPa	1318.2 GPa	3504.1 GPa
400 GPa	361.33 GPa	361.33 GPa	361.33 GPa	1674.6 GPa	1674.6 GPa	4436.3 GPa
500 GPa	380.49 GPa	380.49 GPa	380.49 GPa	1976.8 GPa	1976.8 GPa	5210.1 GPa

3.7. Analysis and Interpretation of Stiffness Eigenvalues

The eigenvalues of the stiffness matrix for $BaTiO_3$ under various pressures (0 GPa to 500 GPa) (Table 6) provide valuable insight into how the material's rigidity evolves in different principal directions[65,66]. At 0 GPa, the three smallest eigenvalues (λ_1, λ_2, λ_3) are each 118.68 GPa, while the intermediate eigenvalues (λ_4, λ_5) are 169.81 GPa, and the largest eigenvalue (λ_6) reaches 460.2 GPa. As pressure increases, these values grow dramatically: for instance, at 500 GPa, the three smallest eigenvalues rise to 380.49 GPa, the intermediate eigenvalues reach 1976.8 GPa, and the largest eigenvalue soars to 5210.1 GPa. This substantial escalation, particularly in the highest eigenvalues, signifies that $BaTiO_3$ becomes far more resistant to deformation in specific principal directions, indicating an increasingly anisotropic mechanical response under compression. From an engineering standpoint, such as in 3D printing structural components, this heightened anisotropy can be advantageous, provided the printing strategy aligns the material's strongest orientations with the most critical load paths[67,68].

Table. 7: Variations of the elastic moduli of $BaTiO_3$ under different pressure levels

	Young's modulus		Linear compressibility		Shear modulus		Poisson's ratio	
	E_{min}	E_{max}	β_{min}	β_{max}	G_{min}	G_{max}	ν_{min}	ν_{max}
0 GPa	215.04 GPa	283.05 GPa	2.173 TPa^{-1}	2.173 TPa^{-1}	84.906 GPa	118.68 GPa	0.10509	0.32491
100 GPa	565.59 GPa	768.61 GPa	0.63111 TPa^{-1}	0.63111 TPa^{-1}	213.99 GPa	305.62 GPa	0.20285	0.41496
200 GPa	749.44 GPa	1267.1 GPa	0.38937 TPa^{-1}	0.38937 TPa^{-1}	276.73 GPa	505.51 GPa	0.16687	0.50813
300 GPa	904.16 GPa	1664.2 GPa	0.28538 TPa^{-1}	0.28538 TPa^{-1}	329.75 GPa	659.08 GPa	0.16102	0.5477
400 GPa	1002.4 GPa	2113.1 GPa	0.22541 TPa^{-1}	0.22541 TPa^{-1}	361.33 GPa	837.3 GPa	0.143	0.59687
500 GPa	1063.8 GPa	2492.3 GPa	0.19194 TPa^{-1}	0.19194 TPa^{-1}	380.49 GPa	988.38 GPa	0.12994	0.63173

3.8. Variations in Elastic Moduli and Their Significance

The second set of data details the minimum and maximum values of Young's modulus, linear compressibility, shear modulus, and Poisson's ratio at each pressure as listed in Table 7[69]. At 0 GPa, Young's modulus ranges from 215.04 GPa to 283.05 GPa, while the shear modulus spans 84.906 GPa to 118.68 GPa. Concurrently, the linear compressibility stands at 2.173 TPa^{-1}, and Poisson's ratio varies from 0.10509 to 0.32491. Under high pressure (500 GPa), Young's modulus surges to a range of 1063.8 GPa to 2492.3 GPa, while the shear modulus increases to 380.49 GPa–988.38 GPa. In parallel, the linear compressibility plummets to 0.19194 TPa^{-1}, indicating the material's pronounced resistance to volumetric deformation. Notably, Poisson's ratio spans an even broader interval of 0.12994 to 0.63173, reflecting both stiff and relatively more flexible responses in different crystallographic directions.

Collectively, these trends underscore the material's transformation into a substantially stiffer, more load-bearing solid with increasing pressure. The broadened range of Poisson's ratio suggests that while certain orientations become extremely rigid, others retain enough ductility to mitigate brittle failure. This balance between high stiffness and directional ductility

is especially valuable in advanced 3D printing applications, where components must endure both compressive and tensile stresses without fracturing. By strategically exploiting these pressure-induced mechanical enhancements, $BaTiO_3$ can be tailored for next-generation manufacturing processes, offering a unique combination of strength, anisotropy control, and structural resilience. The three-dimensional illustrations of the anisotropic elastic properties of $BaTiO_3$ at various pressures (0, 100, 200, 300, 400, and 500 GPa), obtained using the ELATE software[70], are presented in Figure.8. These visualizations provide valuable insights into the pressure-induced evolution of the material's elastic anisotropy.

(a) 0 GPa

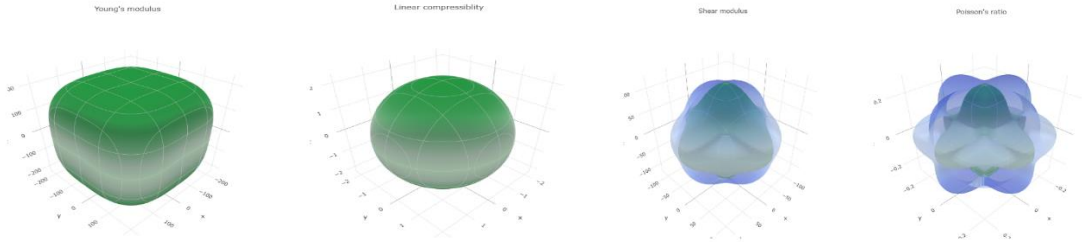

(b) 100 GPa

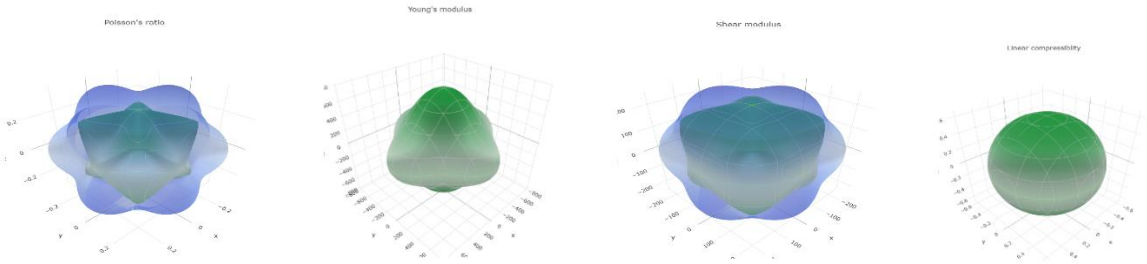

(c) 200 GPa

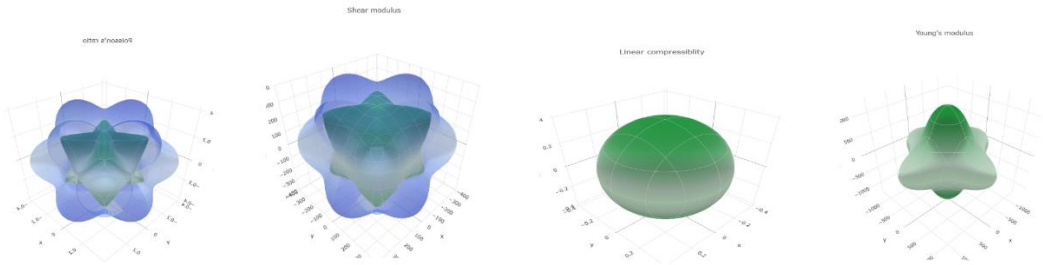

(d) 300 GPa

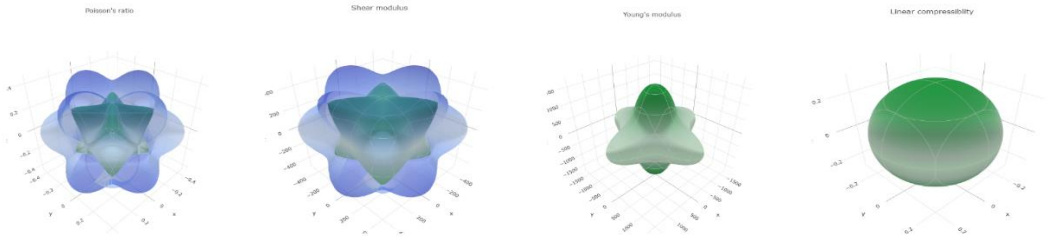

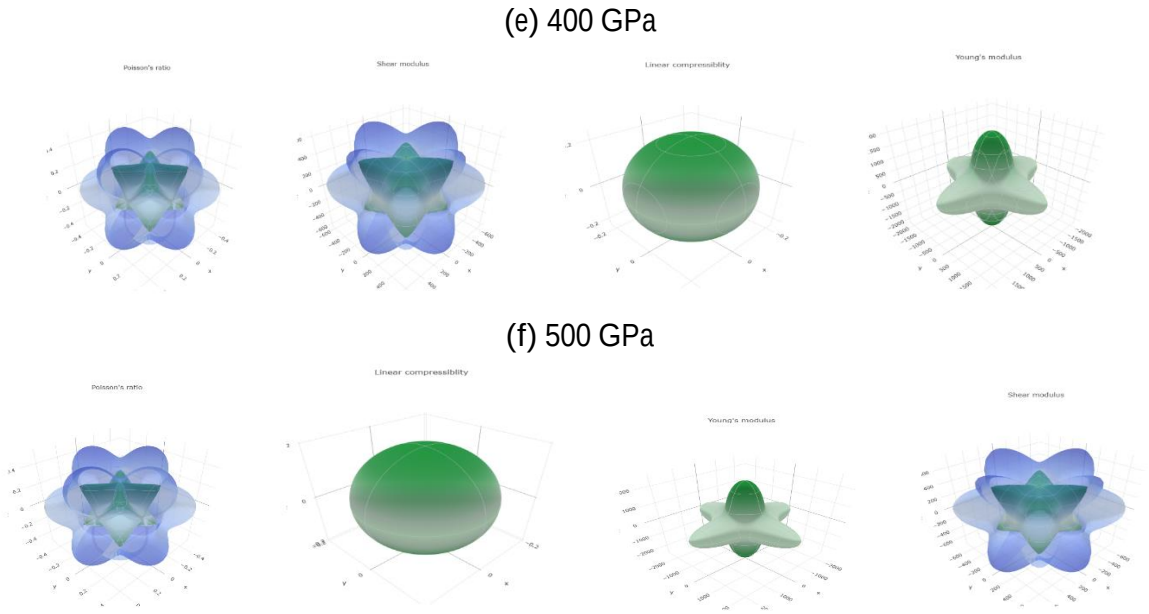

Figure.8: The 3D illustrations of the anisotropic elastic properties of $BaTiO_3$; 0 GPa (a), 100 GPa (b), 200 GPa (c), 300 GPa (d),400 GPa (e), and 500 GPa (f)

4. Solar cell application

$BaTiO_3$ has emerged as a promising material in the field of photovoltaics due to its high dielectric constant, tunable electronic properties, and strong light absorption capabilities[10,71]. The integration of $BaTiO_3$ into solar cells, particularly perovskite-based photovoltaics, has demonstrated improved charge carrier mobility and enhanced stability under external environmental conditions[72]. Moreover, the pressure-induced modifications in the band gap of $BaTiO_3$ provide opportunities to optimize its electronic structure for higher energy conversion efficiency. By understanding the influence of pressure on the electronic and optical properties of $BaTiO_3$, this study contributes to the development of more efficient and durable photovoltaic materials.

The solar cell was designed and simulated using SCAPS-1D software[73]. Figure.9 illustrates the cell's structure, highlighting key components such as IGZO, which serves as the electron transport layer (ETL), and $BaTiO_3$ under varying pressure conditions, functioning as the window layer. The absorber layer consists of $CH_3NH_3PbI_3$, while a flat band model is applied to both the front and back contacts. To ensure the accuracy and reliability of the simulation, the electronic parameters of these layerscritical for evaluating the device's performance were carefully chosen and are detailed in Table 8 [74–77]. These parameters were computed and obtained from well-established literature sources[78].

Table 8: Electronic parameters of used layer in the device structure

Parameters	FTO	IGZO	$BaTiO_3$	$\mathbf{CH_3NH_3PbI_3}$
W(µm)	0.4	0.055	0 .3	0.6
Electron affinity(eV)	9	3.5	3.9	3.9
ε_r(relative)	4	9	2500	10

Parameters	FTO	IGZO	$BaTiO_3$	$CH_3NH_3PbI_3$
$E_g(eV)$	3.5	3.07	1.810	1.56
$N_c(cm^{-3})$	2.2×10^{18}	9.6×10^{19}	2.2×10^{18}	2.76×10^{18}
$N_v(cm^{-3})$	1.8×10^{19}	2.8×10^{19}	1.8×10^{18}	3.9×10^{18}
$\mu_n(cm^2/Vs)$	20	70	20	15
$\mu_p(cm^2/Vs)$	10	20.3	10	15
$N_D(cm^{-3})$	2×10^{19}	10^{18}	10^{16}	0
$N_A(cm^{-3})$	0	0	0	10^{12}

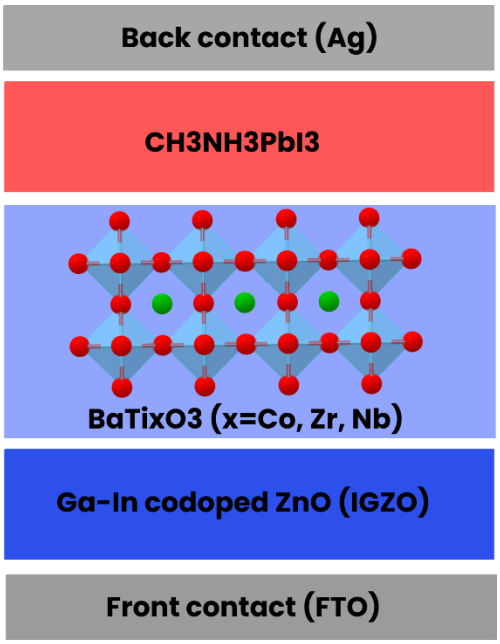

Figure 9. The studied solar cell structure device.

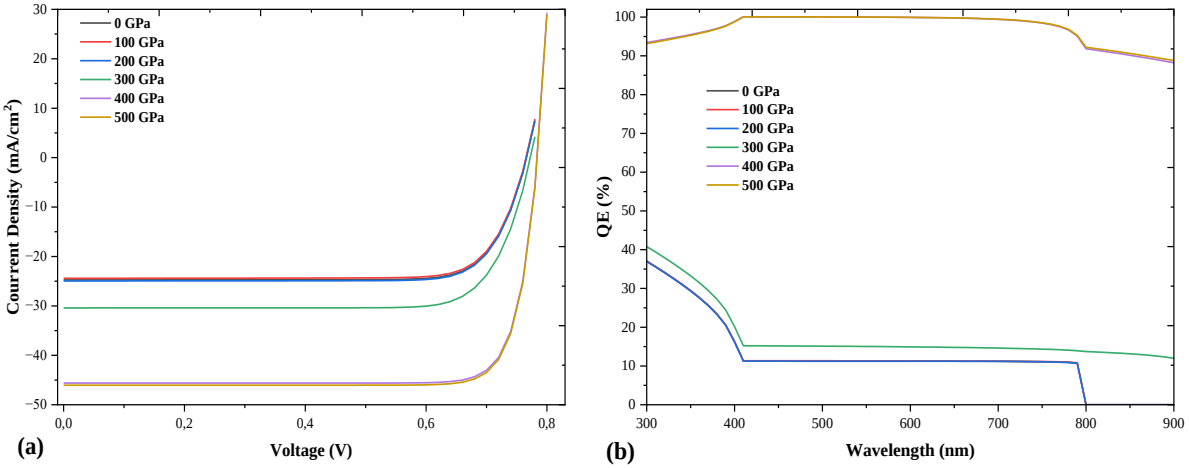

Figure.10. Current Density and Quantum Efficiency QE of $BaTiO_3$ under different pressure levels.

4.1. Interpretation of JV and Quantum Efficiency Curves from SCAPS-1D (Table 9 and Figure.9)

The Figure.10(a) illustrates the J–V characteristics of $BaTiO_3$-based solar cells under different hydrostatic pressures (0, 100, 200, 300, 400, and 500 GPa). As pressure increases, the short-circuit current density (J_{sc}) curve shifts upward, indicating a higher current output at a given voltage. This shift reflects an improved light-absorption capability and enhanced charge-carrier generation, which are consistent with the pressure-induced narrowing of the band gap observed in our electronic structure calculations. Additionally, the open-circuit voltage (V_{oc}) experiences a modest increase at higher pressures, contributing to an overall rise in power conversion efficiency (PCE). The changes in fill factor (FF) are also visible in the shape of the J–V curves, with elevated pressures generally favoring more rectangular (and thus higher FF) curves. The Figure.10(b) presents the external quantum efficiency (QE) as a function of wavelength. At ambient pressure (0 GPa), the QE curve demonstrates a moderate range of photon absorption. Under increased pressure, however, the QE curve extends to longer wavelengths and/or exhibits a higher overall magnitude in the visible to near-infrared region, signifying more efficient photon harvesting. This enhancement directly corresponds to the pressure-driven band gap tuning, which allows $BaTiO_3$ to absorb lower-energy photons that would otherwise pass through at ambient conditions. The improved QE under elevated pressures thus corroborates the significant gains in J_{sc} and, by extension, PCE.

4.2. Interpretation of SCAPS-1D Photovoltaic Performance Results

The photovoltaic performance of $BaTiO_3$-based devices was simulated using SCAPS-1D under various hydrostatic pressures, as summarized in the Table 9 below:

Table 9: Table of photovoltaic performance of $BaTiO_3$ under various pressures.

Pressure (GPa)	PCE (%)	FF (%)	J_{sc} (mA/cm²)	V_{oc} (V)
0	15.23	80.34	24.73	0.7664
100	15.00	80.25	24.41	0.7658
200	15.37	80.36	24.95	0.7667
300	18.65	79.39	30.40	0.7729
400	30.23	84.53	45.61	0.7840
500	30.53	84.54	46.04	0.7843

At ambient conditions (0 GPa), the baseline performance of the $BaTiO_3$ device is modest, with a power conversion efficiency (PCE) of 15.23%, a short-circuit current density (J_{sc}) of 24.73 mA/cm², a fill factor (FF) of 80.34%, and an open-circuit voltage (V_{oc}) of 0.7664 V. These initial values provide a reference point for understanding the impact of applied pressure on device performance. Upon increasing the pressure to 100 and 200 GPa, the photovoltaic parameters remain largely unchanged, indicating that modest pressure does not significantly alter the electronic properties at these levels. However, a noticeable improvement occurs at 300 GPa, where the PCE rises to 18.65%. This enhancement is primarily driven by an increase in Jsc to 30.40 mA/cm² and a slight improvement in V_{oc}, despite a small reduction in FF. The considerable increase in Jsc suggests that the pressure-induced narrowing of the band gap enhances the optical absorption, thereby generating more charge carriers. At higher pressures

(400–500 GPa), the device performance experiences a dramatic boost, with the PCE climbing to over 30% (30.23% at 400 GPa and 30.53% at 500 GPa). In this regime, Jsc nearly doubles to approximately 45.61–46.04 mA/cm^2, and FF increases to around 84.53–84.54%, while Voc exhibits a modest rise to approximately 0.784 V. These improvements underscore the critical role of pressure in tuning the optoelectronic properties of $BaTiO_3$, thereby enabling a more efficient photovoltaic response.

The substantial enhancements in photovoltaic parameters at elevated pressures highlight the dual benefits of pressure engineering: improved light-harvesting capabilities due to band gap modulation and superior charge carrier dynamics. When coupled with the significant mechanical robustness achieved through pressure-induced stiffness improvements, these findings position $BaTiO_3$ as a highly promising material for multifunctional applications particularly in high-performance photovoltaic devices and 3D printing, where both electrical efficiency and mechanical durability are paramount.

5.CONCLUSION

In summary, our comprehensive investigation demonstrates that hydrostatic pressure plays a critical role in tuning the multifunctional properties of $BaTiO_3$. Using all the data presented from the hydrostatic pressure impact on $BaTiO_3$'s structural contraction, band gap modulation, and enhanced photovoltaic performance to the dramatic rise in stiffness and selective anisotropy revealed by the stiffness eigenvalues this work underscores the powerful role of pressure engineering in optimizing $BaTiO_3$ for multifunctional applications. The SCAPS-1D simulations confirm that even moderate pressure levels can substantially improve device metrics such as J_{sc}, FF, V_{oc}, and, ultimately, the power conversion efficiency (PCE). Moreover, the derived stiffness matrices and elastic moduli show a marked increase in Young's modulus, shear modulus, and bulk modulus at elevated pressures, indicating superior mechanical resilience and load-bearing capacity. These improvements hold special relevance for 3D printing technologies, where high structural integrity is required alongside reliable electronic performance. Collectively, our findings illustrate how tuning $BaTiO_3$ via hydrostatic pressure can yield a highly efficient, mechanically robust material suitable for next-generation photovoltaics and advanced additive manufacturing processes. This synergy between optoelectronic and mechanical enhancements not only advances the fundamental understanding of perovskite behavior under extreme conditions but also opens new avenues for tailoring $BaTiO_3$-based systems to meet the demanding requirements of future energy and fabrication technologies.

Funding Declaration: The authors declare that no funds, grants, or other support were received during the preparation of this manuscript.

Data availability statement: The original contributions presented in the study are included in the article/Supplementary Material, further inquiries can be directed to the corresponding author.

Conflict of interest: The authors declare that the research was conducted in the absence of any commercial or financial relationships that could be construed as a potential conflict of interest.

Acknowledgments: The authors would like to extend their profound gratitude to everyone who helped in this scientific endeavor, especially Sultan Moulay Slimane University, and to Prof. Marc Burgelman of the University of Ghent in Belgium for supplying the SCAPS 1-D simulation software.

REFERENCES

[1] *M. Rizwan, Hajra, I. Zeba, M. Shakil, S.S.A. Gillani, Z. Usman, Electronic, structural and optical properties of BaTiO3 doped with lanthanum (La): Insight from DFT calculation, Optik (Stuttg). 211 (2020) 164611. https://doi.org/10.1016/j.ijleo.2020.164611.*

[2] *Z.-X. Chen, Y. Chen, Y.-S. Jiang, DFT Study on Ferroelectricity of BaTiO 3, J. Phys. Chem. B 105 (2001) 5766–5771. https://doi.org/10.1021/jp0032558.*

[3] *V.K. Dwivedi, Fabrication and Ferroelectric Properties of BaTiO 3 Thin Films Deposited on Silicon Substrate Using PLD, Mater. Today Proc. 5 (2018) 9132–9137. https://doi.org/10.1016/j.matpr.2017.10.032.*

[4] *D. Mewada, Barium titanate (BaTiO3): A study of Structural, optical and dielectric properties, Mater. Today Proc. 54 (2022) 923–926. https://doi.org/10.1016/j.matpr.2021.11.252.*

[5] *A. Laassouli, M. Karouchi, A. Ejjabli, H. Errahoui, A. El Haji, Y. Lachtioui, O. Bajjou, Structural, mechanical, electronic, and optoelectronic properties of wide-band-gap hydride perovskite BaNaH3Pt from hybrid density functional theory, Next Materials 11 (2026) 101803. https://doi.org/10.1016/j.nxmate.2026.101803.*

[6] *M.A. Haq, M. Saiduzzaman, T.I. Asif, I.K. Shuvo, K.M. Hossain, Ultra-violet to visible band gap engineering of cubic halide KCaCl 3 perovskite under pressure for optoelectronic applications: insights from DFT, RSC Adv. 11 (2021) 36367–36378. https://doi.org/10.1039/D1RA06430D.*

[7] *M. Szafrański, A. Katrusiak, Photovoltaic Hybrid Perovskites under Pressure, J. Phys. Chem. Lett. 8 (2017) 2496–2506. https://doi.org/10.1021/acs.jpclett.7b00520.*

[8] *O. Mazur, K. Tozaki, Y. Yoshimura, L. Stefanovich, Influence of pressure on the kinetics of ferroelectric phase transition in BaTiO3, Physica A: Statistical Mechanics and Its Applications 599 (2022) 127436. https://doi.org/10.1016/j.physa.2022.127436.*

[9] *M. Karouchi, Y. Lachtioui, O. Bajjou, Transformation of BaTiO3 electro-optical properties through graphene oxide integration for high-performance photovoltaic applications, Mater. Sci. Energy Technol. (2025). https://doi.org/10.1016/j.mset.2025.07.003.*

[10] *L. Fiter, M.N. Mustafa, Y. Sulaiman, Optimization of power conversion efficiency of BaTiO3 as a compact layer in DSSC using response surface methodology/Box-Behnken design, Optik (Stuttg). 288 (2023) 171212. https://doi.org/10.1016/j.ijleo.2023.171212.*

[11] *S. Samine, M. Karouchi, M. Zemzami, N. Hmina, S. Belhouideg, Mechanical properties of 3D-Printed aluminum, nickel, and titanium using a hybrid machine learning and computational mechanics approach, Front. Mater. 12 (2025). https://doi.org/10.3389/fmats.2025.1584896.*

[12] *E.S. Goh, L.H. Ong, T.L. Yoon, K.H. Chew, Structural and response properties of all BaTiO3 phases from density functional theory using the projector-augmented-wave methods, Comput. Mater. Sci. 117 (2016) 306–314. https://doi.org/10.1016/j.commatsci.2016.01.037.*

[13] R.I. Eglitis, Ab initio hybrid DFT calculations of BaTiO3, PbTiO3, SrZrO3 and PbZrO3 (111) surfaces, Appl. Surf. Sci. 358 (2015) 556–562. https://doi.org/10.1016/j.apsusc.2015.08.010.

[14] V.B. Parmar, D. Raval, S.K. Gupta, P.N. Gajjar, A.M. Vora, BaTiO3 perovskite for optoelectronics application: A DFT study, Mater. Today Proc. (2023). https://doi.org/10.1016/j.matpr.2023.01.410.

[15] S.J. Clark, M.D. Segall, C.J. Pickard, P.J. Hasnip, M.I.J. Probert, K. Refson, M.C. Payne, First principles methods using CASTEP, Z. Kristallogr. Cryst. Mater. 220 (2005) 567–570. https://doi.org/10.1524/zkri.220.5.567.65075.

[16] M.D. Segall, P.J.D. Lindan, M.J. Probert, C.J. Pickard, P.J. Hasnip, S.J. Clark, M.C. Payne, First-principles simulation: ideas, illustrations and the CASTEP code, Journal of Physics: Condensed Matter 14 (2002) 2717–2744. https://doi.org/10.1088/0953-8984/14/11/301.

[17] A.A.Z. Munio, A.Q. Liboon Jr., Y.J. Lagud, U.B. Patayon, A.A.G. Pido, M. Karouchi, L.C.C. Ambolode II, A Density Functional Theory Study on the Interaction of Cellulose Biopolymer and Atomic Arsenic, Solid State Phenomena 352 (2023) 39–46. https://doi.org/10.4028/p-pPEfx7.

[18] J.P. Perdew, K. Burke, M. Ernzerhof, Generalized Gradient Approximation Made Simple, Phys. Rev. Lett. 77 (1996) 3865–3868. https://doi.org/10.1103/PhysRevLett.77.3865.

[19] J.M. Del Campo, J.L. Gázquez, S.B. Trickey, A. Vela, Non-empirical improvement of PBE and its hybrid PBE0 for general description of molecular properties, Journal of Chemical Physics 136 (2012). https://doi.org/10.1063/1.3691197.

[20] H.J. Monkhorst, J.D. Pack, Special points for Brillouin-zone integrations, Phys. Rev. B 13 (1976) 5188–5192. https://doi.org/10.1103/PhysRevB.13.5188.

[21] D.C. Liu, J. Nocedal, On the limited memory BFGS method for large scale optimization, Math. Program. 45 (1989) 503–528. https://doi.org/10.1007/BF01589116.

[22] M. Jamal, S. Jalali Asadabadi, I. Ahmad, H.A. Rahnamaye Aliabad, Elastic constants of cubic crystals, Comput. Mater. Sci. 95 (2014) 592–599. https://doi.org/10.1016/j.commatsci.2014.08.027.

[23] D.C. Wallace, J.L. Patrick, Stability of Crystal Lattices, Physical Review 137 (1965) A152–A160. https://doi.org/10.1103/PhysRev.137.A152.

[24] S. Uddin, A. Das, M.A. Rayhan, S. Ahmad, R.M. Khokan, M. Rasheduzzaman, R. Das, A. Ullah, Y. Arafat, M.Z. Hasan, Theoretical prediction of the mechanical, electronic, optical and thermodynamic properties of antiperovskites A3BO (A = K, Rb and B = Au, Br) using DFT scheme: new candidate for optoelectronic devices application, J. Comput. Electron. (2024). https://doi.org/10.1007/s10825-024-02213-1.

[25] M. KAROUCHI, A. EJJABLI, S. SAMINE, O. BAJJOU, Y. LACHTIOUI, Enhancing the Optoelectronic Properties of TiPbO3 perovskite through Lanthanum Doping, Solar Energy and Sustainable Development Journal (2024) 142–155. https://doi.org/10.51646/jsesd.v14iSI_MSMS2E.397.

[26] A. Ejjabli, M. Karouchi, M. Al-Hattab, O. Bajjou, K. Rahmani, Y. Lachtioui, Investigation of lead-free halide K2AgSbBr6 double Perovskite's structural, electronic, and optical properties using DFT functionals, Chemical Physics Impact 9 (2024) 100656. https://doi.org/10.1016/j.chphi.2024.100656.

[27] A. Ejjabli, M. Karouchi, H. Errahoui, O. Bajjou, J. Guerroum, A. Elhajji, K. Rahmani, Y. Lachtioui, Electronic and Optical Properties of Double Perovskite Oxide $LaFeWO_6$: A Theoretical Understanding from DFT Calculations, E3S Web of Conferences 582 (2024) 02001. https://doi.org/10.1051/e3sconf/202458202001.

[28] A. Ejjabli, M. Karouchi, H. Errahoui, A. El Haji, Y. Lachtioui, O. Bajjou, First-principles comparative analysis of the physical properties of K2AgMBr6 (M = Sb, Bi, P, In) perovskites: Promising candidates for clean energy applications, Next Materials 9 (2025) 101321. https://doi.org/10.1016/j.nxmate.2025.101321.

[29] A. Laassouli, M. Karouchi, A. Ejjabli, A. El Haji, H. Errahoui, Y. Lachtioui, O. Bajjou, Novel Insights into the Electric Field-Driven Electronic and Optical Behavior of K2AgSbI6 via DFT, J. Electron. Mater. (2026). https://doi.org/10.1007/s11664-025-12643-7.

[30] M. Karouchi, Y. Lachtioui, O. Bajjou, Transformation of BaTiO3 electro-optical properties through graphene oxide integration for high-performance photovoltaic applications, Mater. Sci. Energy Technol. (2025). https://doi.org/10.1016/j.mset.2025.07.003.

[31] M. Karouchi, O. Bajjou, H. Jabraoui, A. Ejjabli, M. Archi, L. Moulaoui, K. Rahmani, Y. Lachtioui, Increasing Electro-Optical Properties of Perovskite $FAPbI_3$ Under the Effect of Doping by Sn, in: 2023 3rd International Conference on Innovative Research in Applied Science, Engineering and Technology (IRASET), IEEE, 2023: pp. 1–7. https://doi.org/10.1109/IRASET57153.2023.10152963.

[32] A. Laassouli, M. Karouchi, A. Ejjabli, H. Errahoui, A. El Haji, Y. Lachtioui, O. Bajjou, Tuning optoelectronic properties in BaNaH3X (X = Ni, Pd, Pt) perovskite hydrides: a DFT-based analysis, J. Mol. Model. 32 (2026) 39. https://doi.org/10.1007/s00894-025-06624-0.

[33] A.H. Slavney, T. Hu, A.M. Lindenberg, H.I. Karunadasa, A Bismuth-Halide Double Perovskite with Long Carrier Recombination Lifetime for Photovoltaic Applications, J. Am. Chem. Soc. 138 (2016) 2138–2141. https://doi.org/10.1021/jacs.5b13294.

[34] Y.-Q. Zhao, B. Liu, Z.-L. Yu, D. Cao, M.-Q. Cai, Tuning Charge Carrier Types, Superior Mobility and Absorption in Lead-free Perovskite CH3NH3GeI3: Theoretical Study, Electrochim. Acta 247 (2017) 891–898. https://doi.org/10.1016/j.electacta.2017.06.154.

[35] A. Laassouli, M. Karouchi, A. Ejjabli, H. Errahoui, A. El Haji, Y. Lachtioui, O. Bajjou, Structural, mechanical, electronic, and optoelectronic properties of wide-band-gap hydride perovskite BaNaH3Pt from hybrid density functional theory, Next Materials 11 (2026) 101803. https://doi.org/10.1016/j.nxmate.2026.101803.

[36] H. Errahoui, M. Karouchi, A. Ejjabli, A. Elhaji, K. Rahmani, M. Harb, Y. Lachtioui, O. Bajjou, DFT study of optoelectronic properties in pristine and Ba-doped SrH2 for enhanced energy storage and photonic applications, Journal of Materials Science: Materials in Engineering (2026). https://doi.org/10.1186/s40712-026-00405-0.

[37] A. Laassouli, M. Karouchi, A. Ejjabli, A. El Haji, H. Errahoui, K. Rahmani, Y. Lachtioui, O. Bajjou, Halide-driven tuning of structural, electronic, and optical properties in lead-free K2AgSbX6 (X = I, Br, Cl) double perovskites: a DFT study, J. Mol. Model. 32 (2026) 94. https://doi.org/10.1007/s00894-026-06669-9.

[38] H. Errahoui, M. Karouchi, A. Bakour, A. Ejjabli, A. El Haji, A. Laassouli, Y. Lachtioui, O. Bajjou, Tailoring the optoelectronic and photocatalytic properties of MgH2 through Sr and Ca doping for sustainable energy technologies, Chemical Papers (2026). https://doi.org/10.1007/s11696-026-04727-3.

[39] S. Sharma, J. Sharma, Y. Sharma, DFT calculations of electronic and optical properties of SrS with LDA, GGA and mGGA functionals, in: 2016: p. 020095. https://doi.org/10.1063/1.4946146.

[40] H. Errahoui, M. Karouchi, A. Ejjabli, A. El haji, A. Laassouli, O. Ait El Alia, S. Chaji, Y. Lachtioui, O. Bajjou, Impact of Calcium Doping on the Electronic and Optical Characteristics of Strontium Hydride (SrH2): A DFT Study, Atoms 12 (2024) 55. https://doi.org/10.3390/atoms12110055.

[41] N. Hasan, A. Kabir, Theoretical Study of the Structural, Electronic, Mechanical, and Optical of Transition Metal (Mn, Co, and Ni) Doped FrGeI3 Perovskites, n.d.
[42] A. EL Haji, M. Karouchi, A. Ejjabli, H. Errahoui, A. Laassouli, M. Harb, Y. Lachtioui, O. Bajjou, First-principles investigation of structural, mechanical, electronic, optical, and thermodynamic properties of perovskite hydrides XRuH3 (X=Mg, Ca, Sr, Ba) for hydrogen storage, Int. J. Hydrogen Energy 223 (2026) 154379. https://doi.org/10.1016/j.ijhydene.2026.154379.
[43] A. Laassouli, L. Moulaoui, A. Najim, H. Errahoui, K. Rahmani, Y. Lachtioui, O.B. Omar Bajjou, Phosphorus Doping Effects on the Optoelectronic Properties of $K_2AgAsBr_6$ Double Perovskites for Photovoltaic Applications, Solar Energy and Sustainable Development Journal (2024) 1–11. https://doi.org/10.51646/jsesd.v14iSI_MSMS2E.407.
[44] H.J. El-Khozondar, R.J. El-Khozondar, M.M. Shabat, D.M. Schaadt, Solar cell with multilayer structure based on nanoparticles composite, Optik (Stuttg). 166 (2018) 127–131. https://doi.org/10.1016/j.ijleo.2018.04.014.
[45] S. Munir, M.K. Butt, S.A. Aldaghfag, Misbah, M. Yaseen, Nasarullah, M. Nazar, H.H. Somaily, First-principles Calculations to Investigate Emerging Double Perovskites K2NaMoX6 (X=Cl, I) Compounds for Magnetic and Optoelectronic Applications, Physica B Condens. Matter 645 (2022) 414252. https://doi.org/10.1016/j.physb.2022.414252.
[46] A. Ejjabli, M. Karouchi, H. Errahoui, A. Laassouli, A. El haji, Y. Lachtioui, O. Bajjou, Comparative DFT Study of K2AgSbBr6 and K2NaScBr6: Exploring the Role of B'B" Cation Substitution on Material Properties, Atoms 13 (2025) 53. https://doi.org/10.3390/atoms13060053.
[47] A. Laassouli, L. Moulaoui, A. Najim, M. Archi, M. Karouchi, K. Rahmani, Y. Lachtioui, O. Bajjou, Electronic and Optical Properties of Cl-doped $CH_3NH_3SnI_3$ Perovskite: A DFT Study, E3S Web of Conferences 601 (2025) 00013. https://doi.org/10.1051/e3sconf/202560100013.
[48] M. Karouchi, A. Ejjabli, O. Bajjou, J. Guerroum, M. Al-Hattab, M.A. Basyooni-M. Kabatas, K. Rahmani, Y. Lachtioui, Investigating the structural, electronic, and optical properties of the novel double perovskite K2AgBiI6 using DFT, Front. Mater. 11 (2024). https://doi.org/10.3389/fmats.2024.1448400.
[49] A. Laassouli, M. Karouchi, A. Ejjabli, Y. Lachtioui, O. Bajjou, DFT study on K2AgSbI6: Exploring the electronic, optical, and elastic properties of a double perovskite, Solid State Commun. 402 (2025) 115947. https://doi.org/10.1016/j.ssc.2025.115947.
[50] M. Archi, O. Bajjou, k. Rahmani, B. Elhadadi, A comparative ab initio analysis of the stability, electronic, thermodynamic, mechanical, and hydrogen storage properties of SrZnH3 and SrLiH3 perovskite hydrides through DFT and AIMD Approaches, Int. J. Hydrogen Energy 105 (2025) 759–770. https://doi.org/10.1016/j.ijhydene.2025.01.312.
[51] R. Hill, The Elastic Behaviour of a Crystalline Aggregate, Proceedings of the Physical Society. Section A 65 (1952) 349–354. https://doi.org/10.1088/0370-1298/65/5/307.
[52] H. Errahoui, M. Karouchi, A. Ejjabli, A. Laassouli, A. EL Haji, Y. Lachtioui, O. Bajjou, Hydrogen Storage and Energy Applications of H6X2N3Na (X = K; Rb): AIMD and First-Principles Study Approach, J. Electron. Mater. (2026). https://doi.org/10.1007/s11664-026-12736-x.
[53] M. Archi, O. Bajjou, K. Rahmani, B. Elhadadi, Investigation of structural, phonon, thermodynamic, electronic, and mechanical properties of non-toxic XZnH3 (X = Li, Na, K) perovskites for solid-state hydrogen storage: A DFT and AIMD approach, J. Energy Storage 112 (2025) 115492. https://doi.org/10.1016/j.est.2025.115492.

[54] E. Kiely, R. Zwane, R. Fox, A.M. Reilly, S. Guerin, Density functional theory predictions of the mechanical properties of crystalline materials, CrystEngComm 23 (2021) 5697–5710. https://doi.org/10.1039/D1CE00453K.

[55] S.A. Dar, S.A. Khandy, I. Islam, D.C. Gupta, U.K. Sakalle, V. Srivastava, K. Parrey, Temperature and pressure dependent electronic, mechanical and thermal properties of f -electron based ferromagnetic barium neptunate, Chinese Journal of Physics 55 (2017) 1769–1779. https://doi.org/10.1016/j.cjph.2017.08.002.

[56] S.F. Pugh, XCII. Relations between the elastic moduli and the plastic properties of polycrystalline pure metals, The London, Edinburgh, and Dublin Philosophical Magazine and Journal of Science 45 (1954) 823–843. https://doi.org/10.1080/14786440808520496.

[57] H. errahoui, M. karouchi, A. Ejjabli, A. Laassouli, A. El Haji, Y. Lachtioui, O. Bajjou, DFT-based investigation of Ca_2H_3Br and Ba_2H_3I: electronic, optical, and hydrogen storage properties for energy applications, Phys. Scr. (2025). https://doi.org/10.1088/1402-4896/ae2992.

[58] W. Sailuam, I. Fongkaew, W. Busayaporn, R. Klinkla, K. Phacheerak, Influence of pressure on elasticity, mechanical properties, and Li diffusion in battery electrode material LiCoO2: First-principles calculations, Results Phys. 52 (2023) 106788. https://doi.org/10.1016/j.rinp.2023.106788.

[59] E.F. O'Bannon, P. Söderlind, D. Sneed, M.J. Lipp, H. Cynn, J.S. Smith, C. Park, Zs. Jenei, High pressure stability of β-Zr: no evidence for isostructural phase transitions, High Press. Res. 41 (2021) 247–266. https://doi.org/10.1080/08957959.2021.1957863.

[60] B.R. Hunde, A.D. Woldeyohannes, G.A. Workneh, Printing PEDOT:PSS optimized using Response surface method (RSM) and genetic algorithm (ga) via modified 3D printer for perovskite solar cell applications, Appl. Mater. Today 37 (2024) 102134. https://doi.org/10.1016/j.apmt.2024.102134.

[61] H. Karwasara, K.C. Bhamu, S.G. Kang, A.K. Kushwaha, D.P. Rai, S. Sappati, J. Sahariya, A. Soni, Ab-initio investigations for structural, mechanical, optoelectronic, and thermoelectric properties of Ba2SbXO6 (X[dbnd]Nb, Ta) compounds, J. Alloys Compd. 893 (2022). https://doi.org/10.1016/j.jallcom.2021.162332.

[62] S.A. Mir, D.C. Gupta, Structural and mechanical stabilities, electronic, magnetic and thermophysical properties of double perovskite Ba2LaNbO6: Probed by DFT computation, Int. J. Energy Res. 45 (2021) 14603–14611. https://doi.org/10.1002/er.6720.

[63] H. Errahoui, M. Karouchi, A. Ejjabli, A. Laassouli, A. El haji, Y. Lachtioui, O. Bajjou, Photocatalytic Properties of XH2 (X = Ca, Ba, Mg, and Sr): Unlocking Potential for Sustainable Energy and Environmental Applications, Catal. Letters 155 (2025) 359. https://doi.org/10.1007/s10562-025-05193-4.

[64] B. Ali, M.M. Saad H.-E., M.A. Ali, A.A. Alothman, M. Mushab, F. Wadood, J. Ali, S. Hussain, Structural, elastic, mechanical, electronic, and magnetic properties of <scp> In_2NbX_6 </scp> (X = Cl, Br) variant perovskites, Int. J. Quantum Chem. 124 (2024). https://doi.org/10.1002/qua.27294.

[65] F. Mouhat, F.-X. Coudert, Necessary and Sufficient Elastic Stability Conditions in Various Crystal Systems, n.d.

[66] S. Kuma, M.M. Woldemariam, Structural, Electronic, Lattice Dynamic, and Elastic Properties of $SnTiO_3$ and $PbTiO_3$ Using Density Functional Theory, Advances in Condensed Matter Physics 2019 (2019) 1–12. https://doi.org/10.1155/2019/3176148.

[67] S.A. Dar, M.A. Ali, V. Srivastava, Investigation on bismuth-based oxide perovskites MBiO3 (M = Rb, Cs, Tl) for structural, electronic, mechanical and thermal properties, European Physical Journal B 93 (2020). https://doi.org/10.1140/epjb/e2020-10073-x.

[68] M. Husain, N. Rahman, M. Amami, T. Zaman, M. Sohail, R. Khan, A.A. Khan, S.A. Shah, Saeedullah, A. Khan, A.H. Reshak, N.H. Al-Shaalan, S. Alharthi, S.A. Alharthy, M.A. Amin, V. Tirth, Predicting structural, optoelectronic and mechanical properties of germanium based AGeF3 (A = Ga and In) halides perovskites using the DFT computational approach, Opt. Quantum Electron. 55 (2023) 536. https://doi.org/10.1007/s11082-023-04796-8.

[69] A. Ayyaz, G. Murtaza, Y. Bakkour, M. mana Al-Anazy, Impact of Halide Ion Occupancy on Thermodynamic, Mechanical, Electro-optic, and Electron Transport Characteristics of Rb2CuAsX6 (X = F, Cl, Br) Double Perovskites Using Density Functional Theory, J. Inorg. Organomet. Polym. Mater. (2024). https://doi.org/10.1007/s10904-024-03079-3.

[70] R. Gaillac, P. Pullumbi, F.-X. Coudert, ELATE: an open-source online application for analysis and visualization of elastic tensors, Journal of Physics: Condensed Matter 28 (2016) 275201. https://doi.org/10.1088/0953-8984/28/27/275201.

[71] P.-K. Kung, M.-H. Li, P.-Y. Lin, J.-Y. Jhang, M. Pantaler, D.C. Lupascu, G. Grancini, P. Chen, Lead-Free Double Perovskites for Perovskite Solar Cells, Solar RRL 4 (2020). https://doi.org/10.1002/solr.201900306.

[72] F. Ji, G. Boschloo, F. Wang, F. Gao, Challenges and Progress in Lead-Free Halide Double Perovskite Solar Cells, Solar RRL 7 (2023). https://doi.org/10.1002/solr.202201112.

[73] P. Srivastava, Sadanand, S. Rai, P. Lohia, D.K. Dwivedi, H. Qasem, A. Umar, S. Akbar, H. Algadi, S. Baskoutas, Theoretical study of perovskite solar cell for enhancement of device performance using SCAPS-1D, Phys. Scr. 97 (2022) 125004. https://doi.org/10.1088/1402-4896/ac9dc5.

[74] M. Vagadia, A. Ravalia, P.S. Solanki, P. Pandey, K. Asokan, D.G. Kuberkar, Electrical properties of BaTiO3 based - MFIS heterostructure: Role of semiconductor channel carrier concentration, AIP Adv. 4 (2014). https://doi.org/10.1063/1.4880496.

[75] M. Vagadia, A. Ravalia, P.S. Solanki, P. Pandey, K. Asokan, D.G. Kuberkar, Electrical properties of BaTiO3 based - MFIS heterostructure: Role of semiconductor channel carrier concentration, AIP Adv. 4 (2014). https://doi.org/10.1063/1.4880496.

[76] N.H. Yusoff, R.A.M. Osman, M.S. Idris, K.N.D.K. Muhsen, N.I.M. Nor, Dielectric and structural analysis of hexagonal and tetragonal phase BaTiO3, in: AIP Conf. Proc., American Institute of Physics Inc., 2020. https://doi.org/10.1063/1.5142130.

[77] Electrical properties of BaTiO3 based – MFIS heterostructure: Role of semiconductor channel carrier concentration, (n.d.).

[78] Md.A.F. Siddique, A.S.Md. Sayem Rahman, The SCAPS-1D simulation of non-toxic KGeCl3 perovskite from DFT derived properties, Materials Science and Engineering: B 303 (2024) 117268. https://doi.org/10.1016/j.mseb.2024.117268.